

Increasing certainty in projected local extreme precipitation change

Chao Li, Jieyu Liu, Fujun Du, Francis W. Zwiers, & Guolin Feng
2025

Pacific Climate Impacts Consortium (PCIC)

PCIC Publications

© Li, Liu, Du, Zwiers, & Feng. This is an open access article distributed under the terms of the Creative Commons CC BY-NC-ND 4.0 License: <https://creativecommons.org/licenses/by-nc-nd/4.0/>.

Original citation:

Li, C., Liu, J., Du, F., Zwiers, F. W., & Feng, G. (2025). Increasing certainty in projected local extreme precipitation change. *Nature Communications*, 16(1), 850. <https://doi.org/10.1038/s41467-025-56235-9>

Downloaded from UVicSpace Research & Learning Repository

dspace.library.uvic.ca



University
of Victoria

Libraries

Increasing certainty in projected local extreme precipitation change

Received: 24 January 2024

Chao Li^{1,2}✉, Jieyu Liu³, Fujun Du^{1,2}, Francis W. Zwiers^{4,5} & Guolin Feng^{6,7}

Accepted: 13 January 2025

Published online: 20 January 2025

 Check for updates

The latest climate models project widely varying magnitudes of future extreme precipitation changes, thus impeding effective adaptation planning. Many observational constraints have been proposed to reduce the uncertainty of these projections at global to sub-continental scales, but adaptation generally requires detailed, local scale information. Here, we present a temperature-based adaptive emergent constraint strategy combined with data aggregation that reduces the error variance of projected end-of-century changes in annual extremes of daily precipitation under a high emissions scenario by >20% across most areas of the world. These improved projections could benefit nearly 90% of the world's population by permitting better impact assessment and adaptation planning at local levels. Our physically motivated strategy, which considers the thermodynamic and dynamic components of projected extreme precipitation change, exploits the link between global warming and the thermodynamic component of extreme precipitation. Rigorous cross-validation provides strong evidence of its reliability in constraining local extreme precipitation projections.

Extreme precipitation events pose profound threats to natural and societal systems that are often manifested as floods and landslides. As the climate warms, these events are anticipated to become both more frequent and severe almost everywhere over landmasses where their ramifications are deeply felt^{1–5}. Critical adaptation measures mandate precise projections of future precipitation extremes at spatial scales relevant to the operation of natural and societal systems, which are typically regional to local. For instance, to protect infrastructure such as roads, bridges, and drainage systems from increasingly intense downpours, planners need accurate projections of future local precipitation extremes⁶, often with particular emphasis on the potential severe stress that infrastructure may face in the future⁷. While climate models robustly project the intensification of extreme precipitation events over most areas of the world, the precise magnitude of intensification remains highly uncertain^{4,5,8–11}, especially at local scales^{12–14}.

Previous efforts to use observations to constrain future extreme precipitation projections have only considered global or regional scales^{8–11,15–18}, leaving a crucial gap in understanding at impact-relevant local levels that we attempt to address in this study.

The law of thermodynamics provides a first-order basis for understanding the response of extreme precipitation to global warming^{15,19,20}. A warmer atmosphere holds more water vapor thereby allowing more intense precipitation extremes, which suggests that the uncertainty in future extreme precipitation projections for a given emission scenario can be reduced by reducing uncertainty in future warming projections. Recent studies have reduced uncertainties in future projections of precipitation extremes at global to regional scales using the warming observed during recent past decades as an observational constraint^{9–11}. Nevertheless, this simple temperature constraint becomes ineffective when applied to local extreme

¹Key Laboratory of Geographic Information Science, Ministry of Education, East China Normal University, Shanghai, China. ²School of Geographic Sciences, East China Normal University, Shanghai, China. ³College of Atmospheric Sciences, Lanzhou University, Lanzhou, China. ⁴Pacific Climate Impacts Consortium, University of Victoria, Victoria, BC, Canada. ⁵Key Laboratory of Meteorological Disaster, Ministry of Education, Joint International Research Laboratory of Climate and Environment Change, Nanjing University of Information Science and Technology, Nanjing, China. ⁶School of Physical Science and Technology, Yangzhou University, Yangzhou, China. ⁷Laboratory for Climate Studies, National Climate Center, China Meteorological Administration, Beijing, China.

✉ e-mail: cli@geo.ecnu.edu.cn

precipitation projections as the very large influence of unforced internal climate variability obscures the forced extreme precipitation changes at local scales, even under strong external forcing or great warming^{12–14}. Changes in atmospheric circulation also play a substantial role at local scales such that the projected extreme precipitation changes can differ substantially from expectations based on thermodynamics^{21–25}.

Here we show that despite these challenges, the warming observed during recent decades can considerably reduce uncertainty in the projections of future local extreme precipitation changes over almost all of the global land surface and, in fact, most (>90%) of the globe. This is achieved using an adaptive emergent constraint strategy that exploits an analysis of the thermodynamic and dynamic contributions to local extreme precipitation changes, as projected by an ensemble of climate models participating in the Coupled Model Intercomparison Project Phase 6 (CMIP6; Table S1)²⁶. Climate models participating in CMIP6 generally exhibit higher climate sensitivity than their earlier counterparts²⁷, leading to debate about their reliability in projecting future climate^{28,29} and an urgent need to constrain their projections with reliable observations^{30–33}. We focus on constraining changes in annual maximum daily precipitation accumulation during 2071–2100 relative to 1985–2014 that are projected to occur in response to a high emission scenario as represented by the Shared Socioeconomic Pathway 5-8.5 (SSP5-8.5)³⁴ to highlight the potential severe stress infrastructure may face in this century^{6,7}, while also considering projections under the lower SSP2-4.5 and SSP1-2.6 emissions scenarios³⁴.

In this work, we use a physical scaling diagnostic for extreme precipitation intensity²⁰ to decompose the projected extreme precipitation changes into a thermodynamic component due to increases in atmospheric precipitable water and a residual component dominated by changes in atmospheric vertical velocity (referred to as the dynamic component throughout the manuscript). This decomposition, combined with the spatial aggregation of data from ensemble simulations to reduce the noise from unforced internal climate variability, enables the development of an adaptive emergent constraint strategy for local extreme precipitation projections using a simple temperature constraint. We show the physical and statistical underpinnings of this constraint strategy and a rigorous validation of its reliability.

Results

Reducing the influence of unforced internal variability

The influence of unforced internal climate variability is very large at local scales and its low-frequency components can dampen or amplify the forced long-term changes for multiple decades^{12–14,35–37}. As unforced internal climate variability is unpredictable beyond a decade or so³⁷, it has the potential to obscure physically meaningful emergent constraint relationships for externally forced climatic changes, which are most crucial for increasing confidence in future projections. To reduce such negative effects of unforced internal climate variability, we construct local emergent constraint relationships using model simulated annual maximum daily precipitation amounts aggregated from adjacent grid cells and all ensemble members from individual climate models^{13,14} before considering an emergent constraint strategy (Methods). Aggregating data in this way reduces the inter-model variance of the projected changes in total, thermodynamic, and dynamic grid-cell extreme precipitation under the SSP5-8.5 emissions scenario by about 26%, 15%, and 34% on average over the globe, respectively, with even greater reductions for other lower emissions scenarios (Fig. S1). The more pronounced reduction in the uncertainty of the dynamic part of the projected change is in line with the finding that the interannual variability of extreme precipitation is dominated by the interannual variability of vertical air motion during extreme precipitation events³⁸. The aggregation of data from adjacent grid cells

does not induce considerable biases in the estimates of local extreme precipitation changes (Fig. S2).

The reduction of internal variability through data aggregation enables us to increase both the global area with an effective temperature-based emergent constraint on the properties of local extreme precipitation, and the overall strength of the constraint (see Fig. S3 for the SSP5-8.5 scenario). Also, as will become evident, the reduced dynamic uncertainty obtained via data aggregation contributes importantly to the uncertainty reduction in areas with a valid temperature constraint for thermodynamic extreme precipitation changes only. In areas where the temperature constraint fails even for thermodynamic changes, data aggregation provides the entire uncertainty reduction in the projected extreme precipitation changes.

Physical and statistical underpinnings of a temperature constraint

Extreme precipitation is projected to intensify over most of the Earth's surface except for some regions over the subtropical oceans to the west of continents (Fig. 1a). Thermodynamics alone would cause extreme precipitation to increase everywhere, with a notable amount of amplification in polar regions (Fig. 1b) associated with amplified polar warming³⁹ and enhanced poleward moisture transport caused by moisture increases in a warmer climate⁴⁰. In line with previous studies^{21–23}, much of the complex spatial pattern of the total changes has dynamic origins (Fig. 1c vs. Fig. 1a). Similarly, the spatial pattern of uncertainty in the total changes also stems from the dynamic component (Fig. 1f vs. Fig. 1b). The dynamic component generally dominates total uncertainty in the tropics (30°S to 30°N), while thermodynamic and dynamic uncertainties contribute jointly elsewhere (Fig. 1 right panels and Fig. 2).

We consider whether the uncertainties in the projected forced local extreme precipitation changes can be reduced by a temperature constraint based on the observed global warming during recent decades, and where such constraints are found, examine their physical and statistical underpinnings. To that end, we analyze the inter-model correlations between the projected total, thermodynamic, and dynamic changes in local extreme precipitation and the 1971–2020 trend in global mean surface air temperature (GSAT; Methods). The projected total changes in different models under the SSP5-8.5 scenario show statistically insignificant correlations (at a 5% level) with the corresponding model simulated historical GSAT trends over more than half of the Earth's surface (Fig. 3a), confirming that directly constraining local extreme precipitation projections by a temperature constraint is not a globally useful choice, even under a high emissions scenario. As expected, the thermodynamic contributions are strongly correlated with historical GSAT trends across the globe, with a few exceptions limited to the subtropical oceans and continental interior regions (Fig. 3b), which are likely related to circulation induced reductions of atmospheric moisture availability. In striking contrast, the dynamic contributions and historical GSAT trends are uncorrelated over the vast majority of Earth's surface at the 5% significance level (>80% in area; Fig. 3c).

Changes in tropospheric vertical motion promoting extreme precipitation evidently occur for a variety of regionally important reasons, such as the eastward shift of ENSO-driven precipitation^{25,41}, weakening of the Walker circulation⁴², Hadley cell expansion⁴³, poleward shift of the storm tracks⁴⁴, and possibly the rapid response of extreme precipitation-inducing circulations to the direct radiative effects of increases in atmospheric carbon dioxide and aerosols^{45,46}. Clear associations across models between such dynamical changes and historical GSAT change remain to be established. By modulating thermodynamic changes, dynamic processes ultimately affect and may even mask the association between extreme precipitation total changes and historical GSAT trends over large parts of the Earth's surface (Fig. 3a), such as the tropical and subtropical regions, much of

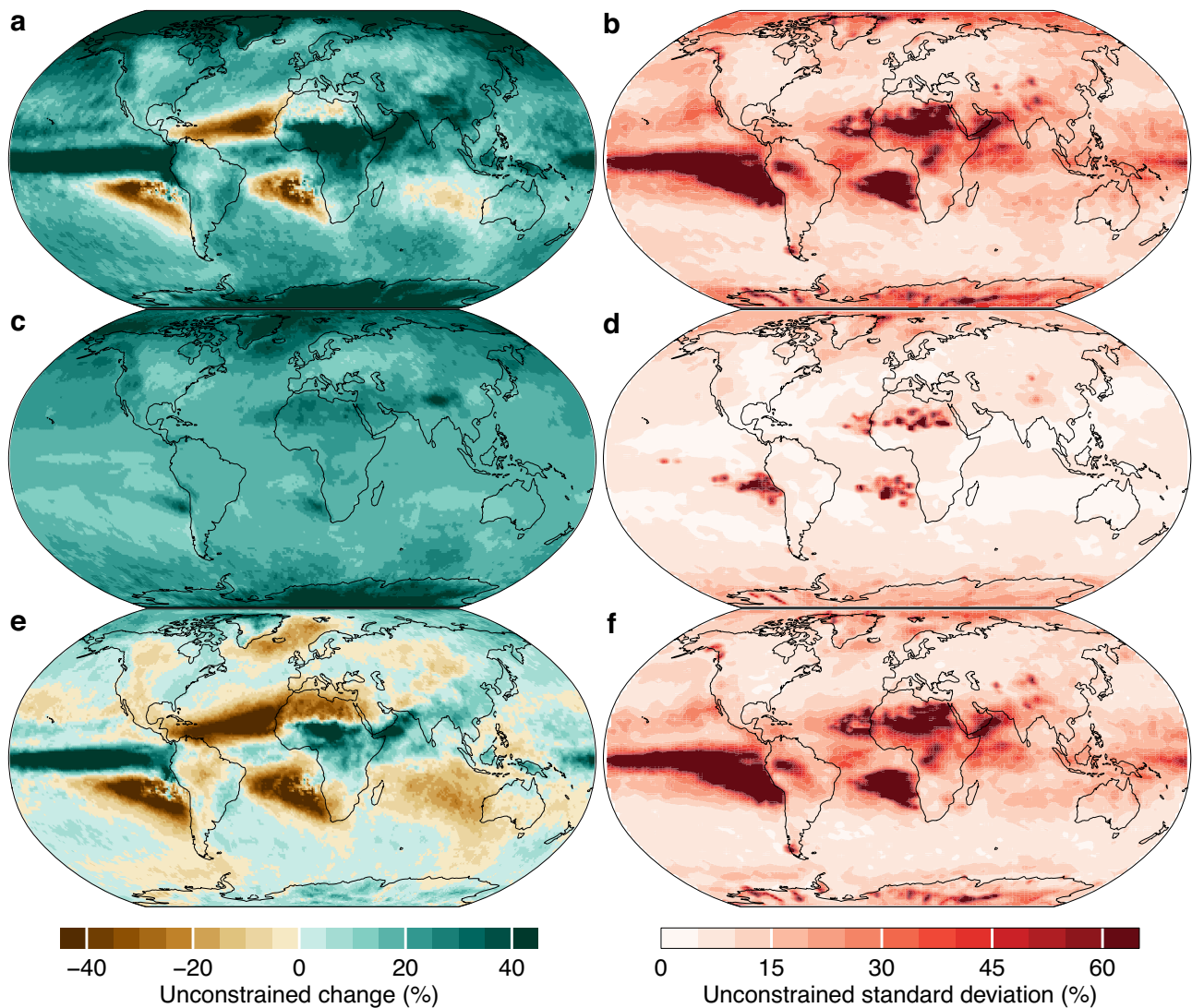


Fig. 1 | Unconstrained projections of future extreme precipitation and uncertainty. The best estimates (in %; left panels) and standard deviations (in %; right panels) of the diagnosed total (a, b), thermodynamic (c, d), and dynamic changes (e, f) in annual maximum daily precipitation during 2071–2100 relative to

1985–2014 under the SSP5-8.5 forcing scenario based on unconstrained CMIP6 multi-model projections (Table S1) to which data aggregation has been applied (Methods).

the continental interior regions, and much of the global ocean (Fig. 3a vs. Fig. 1e). Nevertheless, the dynamic component does enhance the thermodynamic component in some regions and thereby produces stronger inter-model correlations between extreme precipitation total changes and historical GSAT trends in those areas (Methods). One such example is the East Asian monsoon region, where global warming induces secular strengthening of the East Asian summer monsoon^{47,48}.

Under lower emissions scenarios, substantially less areas exhibit statistically significant inter-model correlations between the projected extreme precipitation total changes and simulated historical GSAT trends (Fig. S4), largely due to the relatively larger influence of unforced internal climate variability. This further highlights the limited utility of a simple temperature constraint at local scales. In contrast, the thermodynamic contributions continue to show significant correlations with historical GSAT trends across the global surface (Fig. S4), albeit over smaller areas and with reduced strength, particularly under the SSP1-2.6 scenario (Fig. S4 vs. Fig. 3). Unlike mean precipitation^{49–51} and moderate extreme precipitation^{52–54}, the projected total and thermodynamic changes in annual maximum daily precipitation for a given level of global warming do not strongly depend on emissions

scenarios^{4,54,55} (Fig. S5). In addition to the larger influence of internal climate variability, the reduced constraint correlation under the SSP1-2.6 scenario may indicate that a constraint based on the global mean temperature trend during a historical period of rapid transient response to external forcing could be less effective in scenarios that lead to the stabilization of global mean temperature during the study period 2071–2100 (Fig. S6).

An adaptive emergent constraint on local extreme precipitation

The strong and widespread relationship between the thermodynamic changes in extreme precipitation and historical GSAT trends across emissions scenarios that is underpinned by the law of thermodynamics, and its notable contribution to uncertainties in future local extreme precipitation projections, motivates us to leverage the thermodynamic relationship to reduce these uncertainties, even if as discussed, a temperature constraint is not always effective in constraining the total changes. We propose to constrain the projected total change in local extreme precipitation if there exists a valid emergent relationship for the total change and if the inter-model correlation

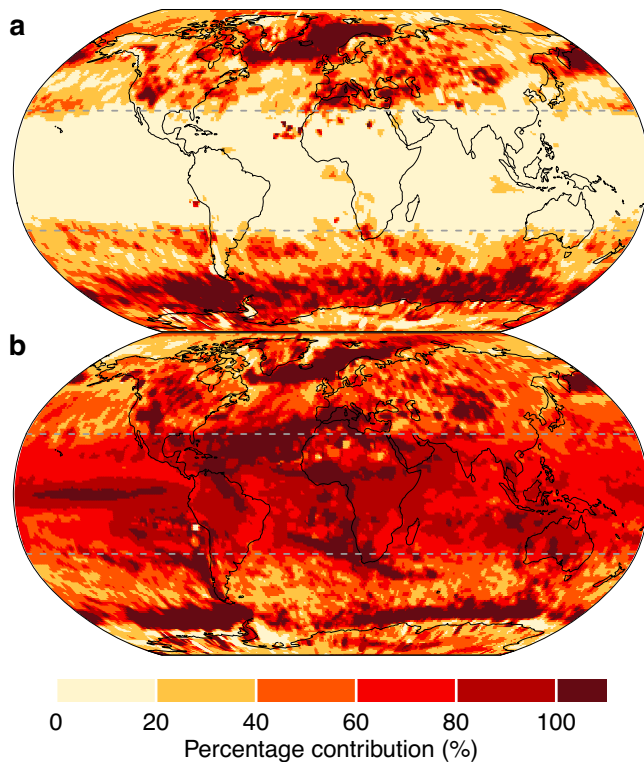


Fig. 2 | Contributions of thermodynamic and dynamic uncertainties to total uncertainty. The percentage contributions of inter-model thermodynamic (a) and dynamic (b) variances to the total variance of the diagnosed changes in annual maximum daily precipitation during 2071–2100 relative to 1985–2014 under the SSP5-8.5 forcing scenario. The percentage contributions can be larger than 100% in regions where the thermodynamic and dynamic changes are negatively correlated. Dashed gray lines mark the latitudes of 30°S and 30°N.

between the thermodynamic and dynamic contributions is positive. A positive inter-model correlation between the thermodynamic and dynamic contributions indicates that the two terms tend to reinforce the emergent relationship for the total change. At locations possessing a valid emergent constraint relationship for the thermodynamic change only, we constrain the projected thermodynamic change and then combine that with the unconstrained projected change in the dynamic component (Methods).

We use a rigorous out-of-sample testing framework^{10,31,33,56} to ascertain the reliability of this temperature emergent constraint strategy in providing more reliable estimates of future local extreme precipitation changes. As future observations are not available, we used each model in turn as pseudo past and future observations, and evaluated whether the constrained projections of future extreme precipitation changes made with the remaining models provide better estimates of the pseudo observations of future changes than unconstrained projections (Methods). The constrained projections are found to have bias that is smaller than, or comparable to, the bias of unconstrained projections except in a few subtropical regions where bias increases (Fig. 4a), and they have noticeably smaller uncertainty virtually everywhere across the constrained Earth's surface (Fig. 4b). Looking to the combination of bias and uncertainty, the constrained projections outperform unconstrained projections over the vast majority of the constrained surface (Fig. 4c). Also, they have central 90% uncertainty intervals that include the pseudo future observations with roughly the expected frequency (i.e., 90%; Fig. S7). Thus, in addition to reducing bias and uncertainty, we conclude that the constrained projections are also generally not overconfident. These results remain robust for the lower emissions scenarios considered,

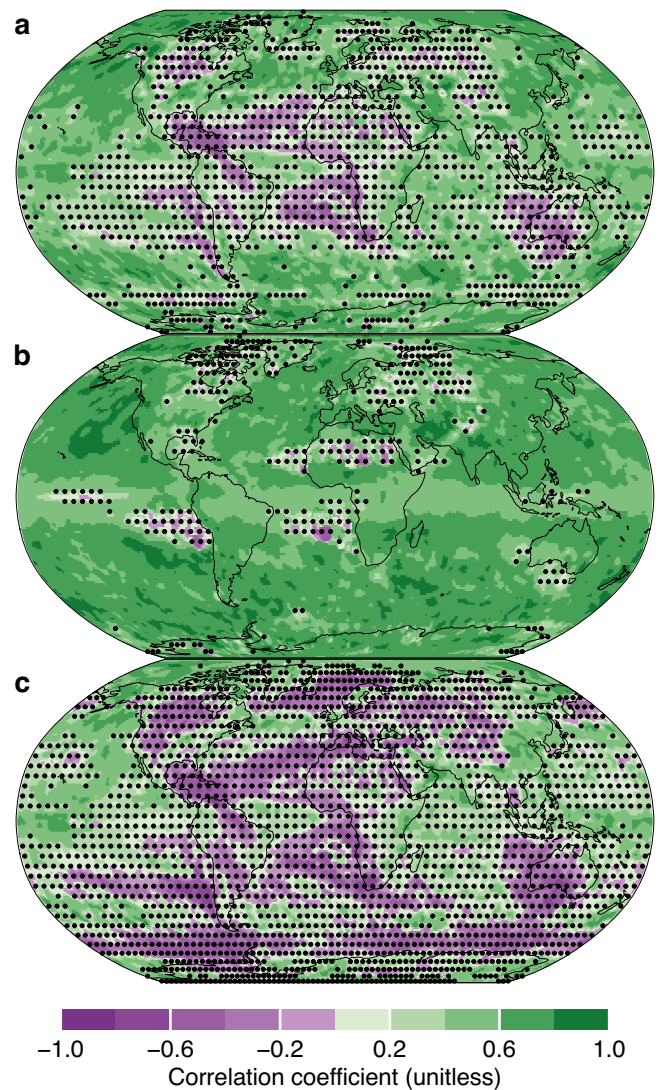


Fig. 3 | Correlations between historical warming and future extreme precipitation changes. The inter-model correlations between the global mean near-surface air temperature trends during 1971–2020 and the diagnosed total (a), thermodynamic (b), and dynamic (c) changes in annual maximum daily precipitation during 2071–2100 relative to 1985–2014 under the SSP5-8.5 forcing scenario. Stippling marks correlations that are not statistically significant at the 5% level. See Fig. S4 for the results under other lower emissions scenarios.

although the reductions in bias and uncertainty are relatively smaller due to the increased influence of unforced internal climate variability (Figs. S7–S8). While subject to uncertainty due to various factors such as the use of an ensemble of opportunity⁵⁷, model interdependency⁵⁸, and exchangeability between models and observations⁵⁹, the cross-validation exercise provides strong evidence of the reliability of our adaptive emergent constraint strategy for extreme precipitation projections at local levels.

Constrained future local extreme precipitation changes

We use the observed 1971–2020 GSAT trend in HadCRUTS⁶⁰ to obtain constrained projections of changes in grid-cell annual maximum daily precipitation during 2071–2100 relative to 1985–2014. External climate forcing during 1971–2020 was dominated by anthropogenic greenhouse gas increases as in the projection period⁶¹. The relatively longer period also helps reduce the impact of internal variability on the constraint relationships³³, particularly mitigating the influence of model-observation discrepancy in the tropical Pacific sea surface

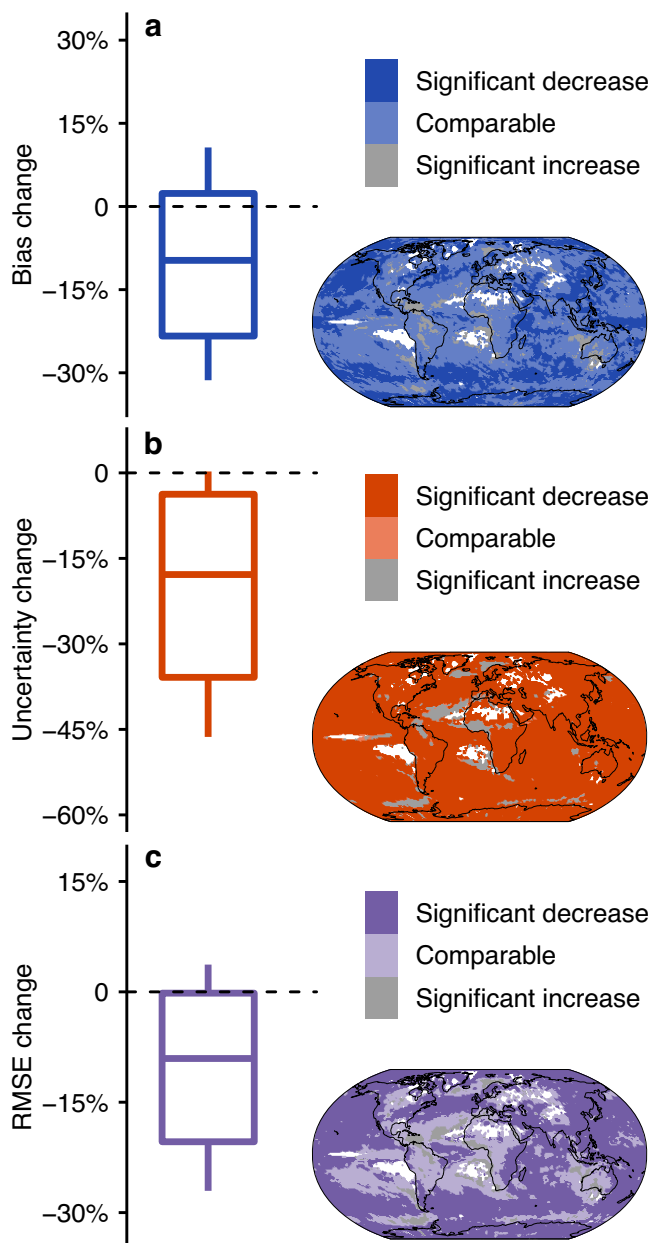


Fig. 4 | Out-of-sample validation of the adaptive emergent constraint method. The percentage differences in bias (a), variance (b) and root mean squared error (c) between the constrained and unconstrained changes in annual maximum daily precipitation during 2071–2100 relative to 1985–2014 under the SSP5-8.5 forcing scenario, as revealed by a model-based cross-validation (see Methods). Boxplots display the multi-model mean percentage differences across grid cells. In each boxplot, the horizontal line and the box represent the median and 16–84% range of the percentage differences, respectively, and the ‘whiskers’ extend to the 5–95% range. At each grid cell, a paired *t*-test is used to determine whether the multi-model percentage differences are significantly different from zero at a 5% level, as marked in the maps. Grid cells where the temperature constraint is not applicable in 80% or more of the considered climate models or scaling diagnostic is significantly biased are left blank. The validation is based on extreme precipitation changes estimated using data aggregation, and thus the bias and uncertainty changes are only due to the application of temperature constraint. See Fig. S8 for the results under other lower emissions scenarios.

temperature trend since 1979⁶². Using another GSAT temperature dataset does not discernably alter the results due to the consistent GSAT trends during the recent past decades in different available global temperature datasets⁶³.

Overall, the spatial patterns of the projected changes and their uncertainties seen in the native model projections are preserved (Fig. 5a vs. Fig. 1a and Fig. 5b vs. Fig. 1b for constrained projections under SSP5-8.5), indicating that the adaptive constraint strategy, although performed at individual grid cells, largely retains the global spatial structure of future extreme precipitation changes as resolved in climate models. Compared to unconstrained projections, the constrained projections indicate globally weaker extreme precipitation changes (Fig. 5c), consistent with first-order expectations based on the difference between observed and simulated historical warming^{27–32,64}. The projected increases in extreme precipitation are reduced by 13% on average across the constrained area, with reductions of 6% or more in 80% of the area. We also find notable uncertainty reductions in the constrained projections globally, with a global median decrease in projection error variance of 18% and decreases of 5% or more in 80% of the constrained area (Fig. 5d).

Including the reduction of internal variability uncertainty achieved by spatial and ensemble data aggregation, the global median total reduction of projection error variance increases to 42%, with reductions of 20% or more across 80% of the constrained area (Fig. 6a). The total uncertainty reduction is calculated by comparing the projection error variance in extreme precipitation changes estimated with data aggregation and then constrained by the temperature emergent constraint strategy to that of unconstrained changes estimated without data aggregation. Thus, for grid cells where the adaptive temperature emergent constraint is not applicable (e.g., stippled grid cells in Fig. 6a), the total uncertainty reduction comes only from the reduced internal variability uncertainty obtained by data aggregation.

The adaptive constraint strategy also suggests globally weaker extreme precipitation changes and smaller error variance in the lower emissions scenarios (Fig. S9). The weakening effect appears more pronounced than in the high SSP5-8.5 scenario, primarily due to the smaller magnitude of unconstrained changes in the lower emissions scenarios. As expected, the weaker temperature constraints for the lower scenarios (Fig. S4 vs. Fig. 3) lead to milder reductions in projection uncertainty, especially for the SSP1-2.6 scenario (Fig. S9 vs. Fig. 5). Nevertheless, the total reduction of error variance is comparable to or even greater than that observed in the SSP5-8.5 scenario (Fig. S10 vs. Fig. 6). This is consistent with the finding that unforced internal variability has a greater influence on extreme precipitation projections when the external forcing is weak (Fig. S1)^{13,65,66}.

The adaptive temperature emergent constraint strategy is similarly effective for seasonal precipitation extremes. Significant temperature constraint correlations are found for the projected thermodynamic changes in seasonal maximum daily precipitation for 2071–2100 under SSP5-8.5 over more than 80% of the global surface (at the 5% level; Fig. S11). The temperature constraint similarly weakens seasonal extreme precipitation projections and reduces projection uncertainties (left and middle panels in Fig. S12), achieving a global median error variance reduction of 13% to 15% across boreal seasons. When combined with the reduction of internal climate variability, the global median total error variance reduction exceeds 40% for all seasons (right panels in Fig. S12).

Discussion

Climate adaptation is drawing increasing attention as societies awaken to the devastating impacts of human caused climate change. Adaptation to future precipitation extremes generally requires local-scale projections of externally forced extreme precipitation changes. Such projections remain uncertain, however, due in large measure, to a combination of internal climate variability and model uncertainty. That uncertainty affects adaptation costs and feasibility, and thus any reduction in the uncertainty of future extreme precipitation projections at impact-relevant scales would be beneficial. Our results show that the projections of future grid-cell extreme precipitation changes

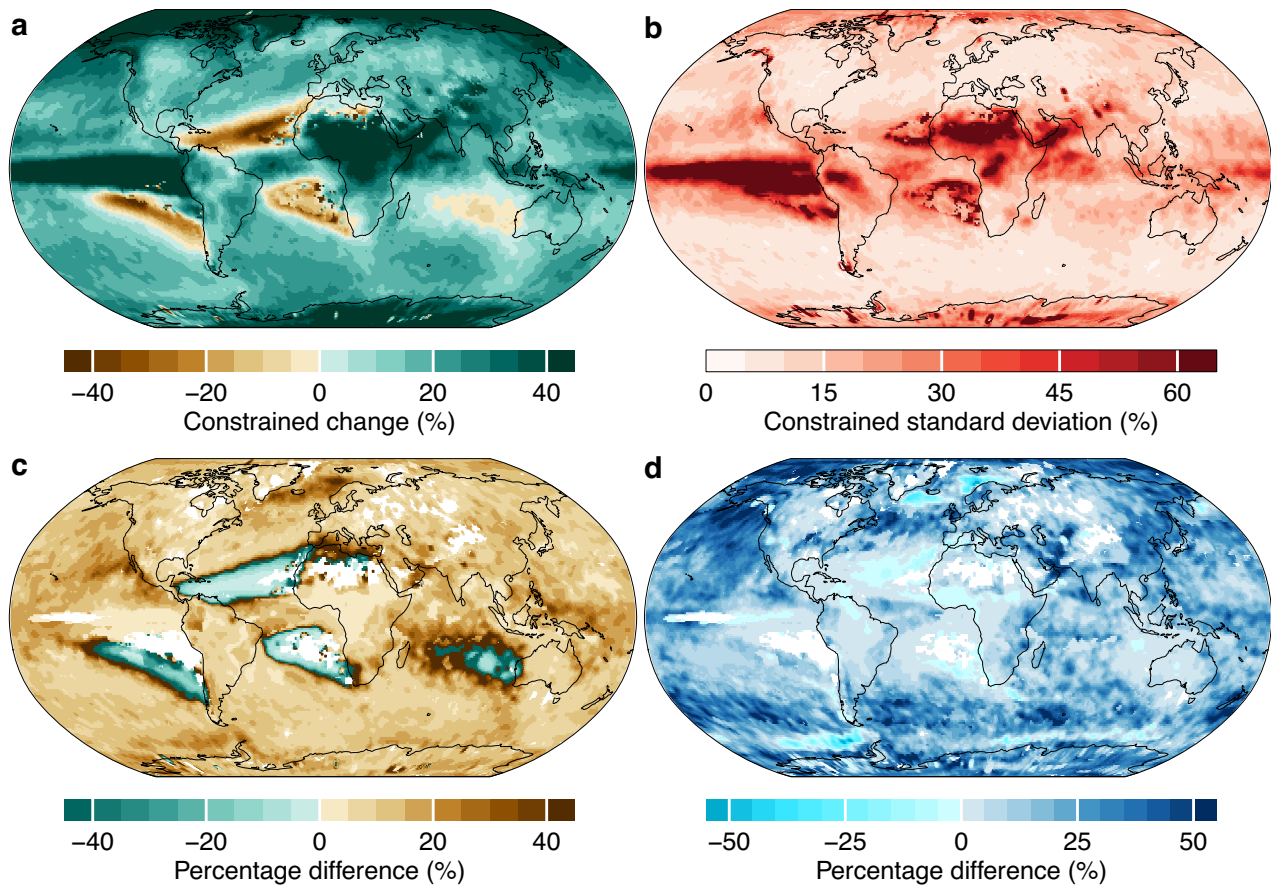


Fig. 5 | Constrained projections of future extreme precipitation and uncertainty. The constrained best estimates (in %; **a**) and standard deviations (in %; **b**) of projected changes in annual maximum daily precipitation during 2071–2100 relative to 1985–2014 under the SSP5-8.5 forcing scenario by CMIP6 climate models. The percentage differences in the best estimates (**c**) and variances (**d**) of the constrained changes relative to those of unconstrained changes estimated with data

aggregation. Grid cells where the temperature constraint is not applicable are filled with unconstrained values in (**a**, **b**) and left blank in (**c**, **d**). Bias and uncertainty differences presented in (**c**, **d**) are achieved solely by the temperature emergent constraint and do not include changes due to the application of data aggregation. See Fig. S9 for the results under other lower emissions scenarios.

can be robustly constrained over the globe with a validated adaptive emergent constraint strategy that uses the observed warming and data aggregation. Globally, the temperature constraint projects end-of-century changes in annual maximum daily precipitation amount under a high SSP5-8.5 forcing scenario that are 13% smaller than raw, unconstrained projections, with an 18% reduction in projection error variance. Combined with the effect of data aggregation in reducing internal variability uncertainty, this error variance reduction increases further to 42%.

These improved projections together with our validation of their reliability should provide more confident insights into the potential risks and stresses that natural and societal systems may face during this century. By permitting more accurate impact assessment and adaptation planning, they are expected to benefit nearly 90% of the world population⁶⁷ (with total uncertainty reduction of >20%; blue bars in Fig. 6b). Specifically, for East and South Asia, which is the home to over 40% of the world's population experiencing climatological heavy monsoon rainfall, the constrained annual maximum daily precipitation projections by late this century are 30% less uncertain (15–70% for 5–95% spatial range) as indicated by total uncertainty reduction. The pronounced uncertainty reductions in regions containing many of the world's largest cities and economic hubs can provide support for advancing climate resilience in these globally important urban areas (Fig. 7).

It should, however, be recognized that while our cross-validation against pseudo-observations of future extreme precipitation from

global climate models increases confidence in the constrained projections, they remain subject to the limitations of both resolution and process representation in contemporary global climate models^{2–5,68} and thus the realism with which the global models simulate extreme precipitation events and their changes in response to future emissions scenarios. This inherent uncertainty should be carefully considered when using the constrained local extreme precipitation projections for infrastructure adaptation and resilience planning. Moreover, the temperature-based constraint primarily targets and eliminates bias and uncertainty in the projected extreme precipitation changes that are directly or indirectly associated with the projected warming or model transient climate response uncertainty.

Further improvement remains desirable in both the tropical and extra-tropical regions. A temperature-based emergent constraint is largely ineffective for the forced extreme precipitation changes in the tropics due to the very large dynamic uncertainties. The dynamic uncertainty is also an important component of the total extreme precipitation projection uncertainty in extratropical regions, with magnitudes that rival or exceed uncertainty in the thermodynamic component of extreme precipitation. Thus, further improvement will ultimately require improvement in simulating the dynamical responses of extreme precipitation to external forcing and the identification of effective emergent constraints for atmospheric circulation changes relevant for extreme precipitation.

Despite the remaining challenges, our adaptive emergent constraint method represents an important advance beyond existing

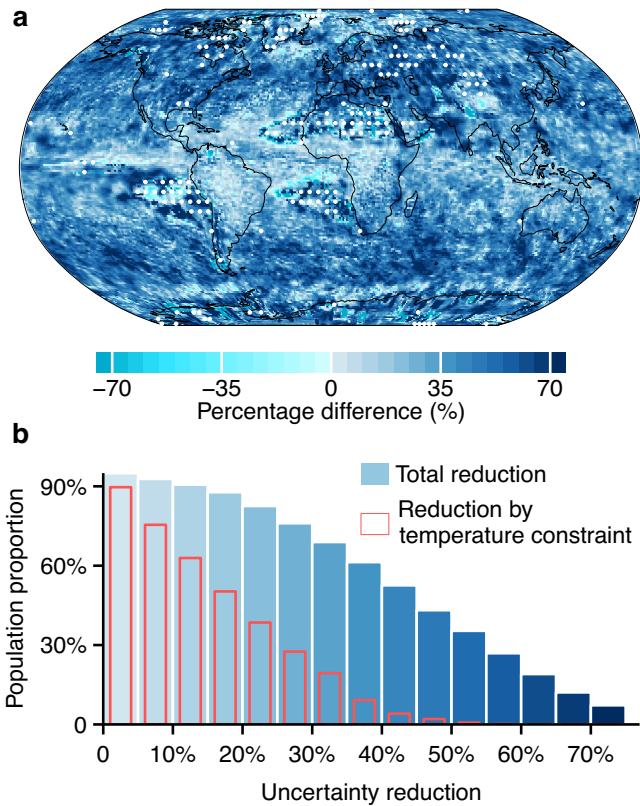


Fig. 6 | Total uncertainty reduction in the constrained projections of future extreme precipitation. **a** The percentage differences in the variances of the constrained changes in annual maximum daily precipitation during 2071–2100 relative to 1985–2014 under the SSP5-8.5 forcing scenario compared to those of unconstrained changes estimated without data aggregation (i.e., using data from individual grid cells and a single simulation member of a climate model) and thus with high unforced internal climate variability. Stippling marks areas where the adaptive temperature emergent constraint is not applicable, and the uncertainty reduction, if any, comes completely from the reduced internal variability uncertainty obtained by data aggregation. **b** The proportions of the global population (in the year 2020) residing in grid cells where the total uncertainty reduction is above the levels marked along the horizontal axis. The corresponding population proportions for uncertainty reduction achieved by the temperature emergent constraint alone are shown by red empty bars. See Fig. S10 for the results under other lower emissions scenarios.

counterparts for mean or extreme precipitation averaged over the globe or large regions that are too coarse to be relevant for locally tailored climate change adaptation and resilience planning. Our results suggest that future adaptation investments to limit the risks from extreme precipitation and related hazards can be better planned at finer local levels with observationally constrained projections as reported here. Moreover, the proposed strategy of pinpointing effective emergent constraints by decomposing the key components of climate change governed by distinct processes offers an attractive pathway for developing observational constraints on low signal-to-noise climate projections.

Methods

Climate model simulations, observations, and gridded world population

We analyze the daily output of 22 climate models participating in CMIP6²⁶ with necessary output (Table S1). We consider the simulated changes in the climatological mean annual maximum daily precipitation accumulation from the historical period 1985–2014 to late this century 2071–2100 forced by the Shared Socioeconomic Pathway 5-8.5

(SSP5-8.5) emissions scenario as well as the moderate SSP2-4.5 and low SSP1-2.6 scenarios³⁴. We extract annual maximum daily precipitation accumulation for each year of the two periods and the associated surface pressure as well as vertical profiles of daily mean air temperature and vertical wind velocity.

We also calculate the modeled trends in GSAT during 1971–2020 from these models to determine emergent constraint relationships for future extreme precipitation changes. We use the GSAT trend during 1971–2020 as the constraint variable because global aerosol radiative forcing varied slowly during this period⁶¹, implying that climate change during this period was primarily driven by greenhouse gas increases as in the projection period. Using a relatively longer period than in many previous studies also help reduce the negative impact of unforced internal climate variability on the constraint relationships for forced changes. We derive the observed GSAT trend from the HadCRUT5 dataset⁶⁰. Using other datasets produces nearly identical GSAT trends in recent decades⁶³. Preindustrial control simulations are used to estimate internal variability uncertainty in the observed GSAT trend, as will be further discussed.

To exemplify the potential benefits of reducing uncertainty in local extreme precipitation projections to stakeholders, we consider the global population in the year 2020 from the 1° × 1° Gridded Population of the World dataset, Version 4, provided by the Center for International Earth Science Information Network at Columbia University⁶⁷.

Physical diagnostic for extreme precipitation changes

Based on a physical scaling diagnostic for extreme precipitation²⁰, the climatological mean annual maximum daily precipitation accumulation during a given period can be approximated as

$$\bar{P} \approx \bar{P}_s = \frac{1}{g} \left\langle \bar{\omega} \times \frac{dq_s}{dp} \Big|_{\theta^*} \right\rangle \quad (1)$$

where $\langle \cdot \rangle$ denotes mass-weighted vertical integration over the troposphere, overbar indicates a time average over the period, g is the acceleration due to gravity, ω is the pressure velocity of vertical wind on the day of extreme precipitation, and $\frac{dq_s}{dp} \Big|_{\theta^*}$ is the derivative of saturation specific humidity q_s at saturation equivalent potential temperature θ^* . Using Eq. (1), changes in the climatological mean annual maximum daily precipitation accumulation between two periods can be approximated as

$$\Delta \bar{P} \approx \Delta \bar{P}_s = \frac{1}{g} \left\langle \Delta \bar{\omega} \times \Delta \frac{dq_s}{dp} \Big|_{\theta^*} \right\rangle \quad (2)$$

where Δ denotes change between two periods and all other terms hold with the same meanings as in Eq. (1). We calculate the thermodynamic contribution $\Delta \bar{P}_{s,ther}$ by replacing $\Delta \bar{\omega}$ with the 1985–2014 baseline mean vertical wind profile $\bar{\omega}$,

$$\Delta \bar{P}_{s,ther} = \frac{1}{g} \left\langle \bar{\omega} \times \Delta \frac{dq_s}{dp} \Big|_{\theta^*} \right\rangle \quad (3)$$

and refer to the remaining change

$$\Delta \bar{P}_{s,dyn} = \Delta \bar{P}_s - \Delta \bar{P}_{s,ther} \quad (4)$$

as the dynamic contribution as it is dominated by changes in extreme ascent. This decomposition has been widely used in understanding extreme precipitation changes in response to anthropogenic climate change^{9-11,21-24}. For each individual climate simulation, we diagnose at each grid cell the total, thermodynamic, and dynamic changes in the climatological mean annual maximum daily precipitation accumulation during 2071–2100 relative to 1985–2014 under different emissions scenarios.

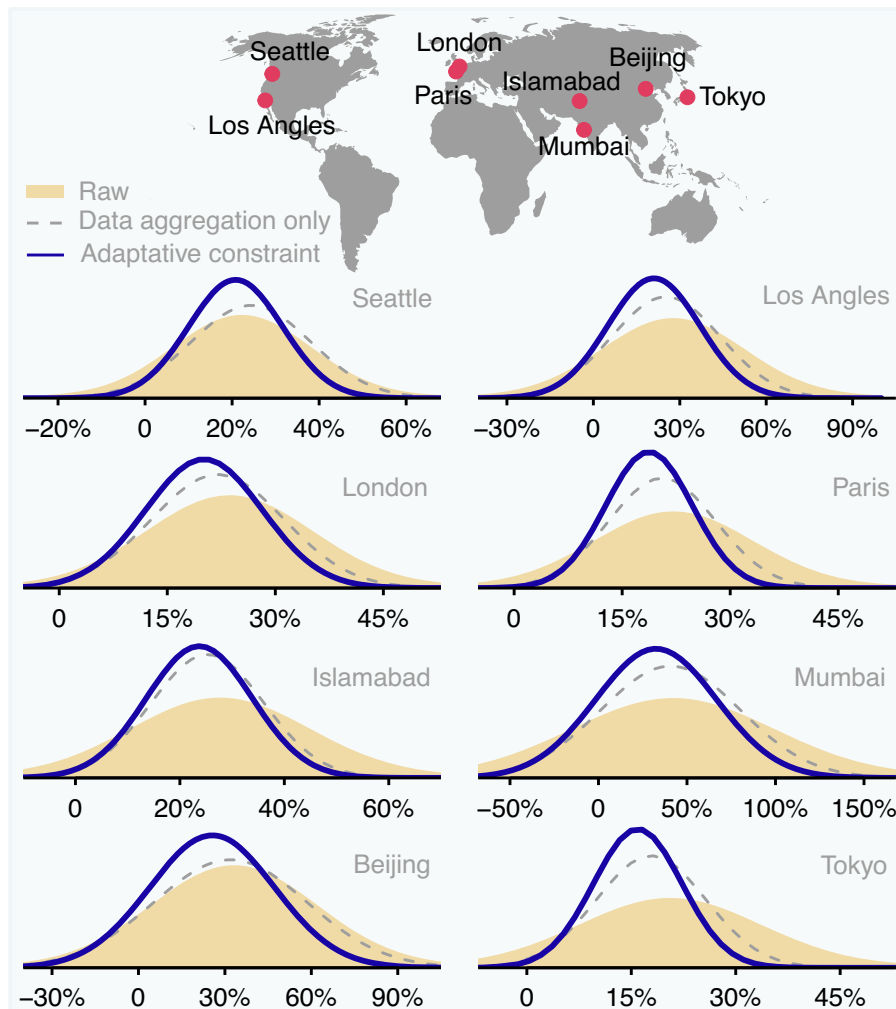


Fig. 7 | Constrained projections of future extreme precipitation for selected grid cells. Panels show the probability distributions of the projected changes in annual maximum daily precipitation during 2071–2100 relative to 1985–2014 under the SSP5-8.5 forcing scenario for grid cells containing the selected large cities

marked on the map, based on unconstrained projections without data aggregation (yellow), unconstrained projections with data aggregation (gray), and constrained projections obtained by applying the adaptive temperature emergent constraint to unconstrained projections with data aggregation (blue).

To facilitate analysis of the diagnosed changes from different climate models with different spatial resolutions, we re-grid all the diagnosed changes to the $1^\circ \times 1^\circ$ grid of the world population dataset, which is also the average spatial resolution of the considered climate models. The diagnosed change $\Delta \bar{P}_s$ differs slightly from the full model simulated change $\Delta \bar{P}$ because it does not account for the change in precipitation efficiency^{20,21}. Nevertheless, the diagnosed and full percentage changes, i.e., $\Delta \bar{P}_s / \bar{P}_s$ vs $\Delta \bar{P} / \bar{P}$, are exchangeable in distribution in the models we considered according to a two-tailed K-S test conducted at 5% significance level (Fig. S13), suggesting that changes in precipitation efficiency do not figure extensively in the projected relative changes of the diagnosed versus full model simulated extreme precipitation. We therefore adopt the physical scaling diagnostic to estimate future annual maximum daily precipitation changes.

Data aggregation to reduce unforced internal variability uncertainty

Unforced internal climate variability in the climate system is unpredictable beyond a decade or so^{35–37}. Internal variability in local extreme precipitation is large and can induce relatively long-term changes that may be confounded with externally forced changes^{12–14}, which may in turn obscure the identification of physically meaningful emergent constraint relationships for the forced changes. In order to reduce the

effects of internal climate variability in local extreme precipitation on derived quantities, we average the diagnosed changes within 3×3 grid cell regions centered on a given grid cell as well as those from all available initial-condition simulation members of a climate model to obtain diagnosed changes for that grid cell and model. The spatial data aggregation helps reduce the influence of high-frequency internal climate variability at small spatial scales^{4,13,14}, while the ensemble aggregation helps reduce the influence of internal climate variability at various time scales, with the extent of the reduction depending on the number of available initial-condition simulations by individual models^{35,69}.

The resulting estimates of extreme precipitation changes remain subject to different degrees of uncertainty of internal variability because different models have different sizes of initial-condition ensembles (Table S1). The remaining internal climate variability uncertainty can be substantial in the moderate and low emissions scenarios. Nevertheless, aggregating across adjacent locations and ensemble members helps reduce the influence of internal variability on the estimation of emergent constraint relationships. Increasing the size of the area for spatial aggregation could further reduce uncertainty from high frequency internal variability, but at the cost of biasing the estimated extreme precipitation changes for individual grid cells¹³. The 3×3 grid cell aggregation strategy does not introduce

significant biases in the estimates of grid cell extreme precipitation changes at the vast majority of individual grid cells, as confirmed by paired t-tests at the 5% level (Fig. S2).

By filtering out as much unforced internal climate variability as possible, our approach essentially focuses on constraining externally forced change in the mean of the extreme precipitation distribution. Although it would be desirable to constrain the entire extreme precipitation distribution that is additionally affected by internal climate variability, we can more confidently constrain how external forcing shifts the distribution than both its position and shape. Confidently constraining projected change in an extreme upper point of precipitation distribution, such as the magnitude of 100-yr events, is possible at regional scale¹⁰, remains to be achieved at a local scale.

Emergent constraints to reduce model response uncertainty

Using the recent 5-decade warming trend as an observational constraint, our adaptive emergent constraint strategy constrains the projected extreme precipitation total change at grid cells where there are (1) statistically significant emergent constraint relationships for the total changes and (2) positive inter-model correlations between the thermodynamic and dynamic contributions. At locations having a valid emergent constraint relationship for the thermodynamic change only, we constrain the thermodynamic change and then combine that with the unconstrained dynamic change. Elsewhere, the temperature constraint is not effective, and the estimated total extreme precipitation changes by data aggregation is used. We note that a positive inter-model correlation between the thermodynamic and dynamic changes indicates that the dynamic changes tend to reinforce the thermodynamic changes in the climate model ensemble, leading to a strengthened emergent relationship for the total change. In this case, constraining the total change provides a greater uncertainty reduction than constraining the thermodynamic change only (Fig. S14).

A schematic flow of the adaptive constraint strategy can be found in Fig. S15. At each grid cell, the constraint configuration involves two sequential statistical tests. The first test evaluates whether the inter-model correlation between the historical warming trend and future extreme precipitation total change is positive at a given significance level, while the thermodynamic and dynamic components interact positively. The second test evaluates whether the inter-model correlation between the historical warming trend and the thermodynamic change is positive at a given significance level. In general, increasing the significance level expands the constrained area and the area where the temperature constraint applies to total change (Fig. S16a vs S16b). The reliability of the constraint configuration depends on both the type I and type II error rates of the two tests. The former refers to applying a constraint in circumstances when the constraint would be ineffective, while the latter refers to failing to apply a constraint when it would be effective. Type I errors therefore have little impact, while type II errors lead to unconstrained local projections that could have been constrained.

We optimized the overall reliability of the adaptive constraint strategy by analyzing the global root mean squared error (RMSE) of constrained extreme precipitation projections with different significance levels in a model-based cross-validation framework, which will be detailed later. Overall, the global mean RMSE reduction increases with larger significance levels and then plateaus (Fig. S16c), suggesting that incorrect constraint configuration decisions associated with these varying significance levels have little impact on the performance of the constraint strategy. We believe that this robustness is ensured by the solid thermodynamic foundation of extreme precipitation intensification. Based on these results, we chose a 10% significance level for the involved statistical testing as a reasonable trade-off that reduces the impact of type II errors on projection bias and variance while not making type I errors excessively often.

We constrain extreme precipitation changes with a hierarchical emergent constraint method⁷⁰ using the 1971–2020 GSAT trend in HadCRUT5, X_{Obs} , as the observational constraint. The method uses a Gaussian distribution with mean and variance given as

$$\mu = \bar{Y} + \frac{\rho\sigma_Y\sigma_X}{\sigma_X^2 + \sigma_{X_{\text{Obs}}}^2} (X_{\text{Obs}} - \bar{X}) \quad (5)$$

$$\sigma^2 = \sigma_Y^2 \left(1 - \frac{\rho^2}{1 + \sigma_{X_{\text{Obs}}}^2 / \sigma_X^2} \right) \quad (6)$$

to represent the constrained extreme precipitation total or thermodynamic changes, where \bar{Y} and σ_Y^2 are the multi-model ensemble mean and variance of the diagnosed total or thermodynamic changes, \bar{X} and σ_X^2 are the corresponding values of the simulated GSAT trends during 1971–2020, ρ is the correlation coefficient describing the strength of the emergent constraint relationship, and $\sigma_{X_{\text{Obs}}}^2$ represents the uncertainty in X_{Obs} .

The observed GSAT trend is affected mainly by two sources of uncertainty, that is, internal climate variability and observational uncertainty. The spread of GSAT trends amongst the HadCRUT5 ensemble members provide information about observational uncertainty⁶⁰. This source of uncertainty is small compared to internal climate variability (0.01 °C vs. 0.14 °C for standard error of the 1971–2020 GSAT trend estimates due to observational uncertainty and internal variability uncertainty). We therefore consider uncertainty in X_{Obs} due to internal climate variability and estimate that uncertainty from preindustrial control simulations of climate models (Table S1). We clarify that the Gaussian distribution is suitable to model the long-term changes in the climatological (multi-decadal mean) annual maximum daily precipitation and the thermodynamic contributions, as supported fundamentally by the statistical central limit theorem⁷¹ and confirmed empirically by a statistical test (Fig. S17).

The hierarchical emergent constraint method does not directly adjust the projected changes from individual climate models, but rather calibrates the overall distribution of the projected changes⁷⁰. For grid cells where the thermodynamic changes are constrained, the constrained changes for individual models are needed to reconstruct the constrained total changes as the sum of the constrained thermodynamic changes and unconstrained dynamic changes from individual models. We obtain the individual constrained thermodynamic changes with a quantile mapping process that maps the unconstrained thermodynamic changes to the quantiles of the constrained distribution based on the probabilities of the corresponding unconstrained changes in the unconstrained distribution (see an illustration of the procedure in Fig. S18). By doing so, the mapped quantiles, that is, the individual constrained thermodynamic changes, retain properties of the constrained distribution.

Model-based out-of-sample validation of the emergent constraint method

Because future observations are not available, we employ a model-based cross-validation approach^{10,31,33,56} to verify that the adaptive temperature emergent constraint strategy can more reliably estimate future local extreme precipitation changes. Specifically, we use each model in turn as pseudo-observations of the past and future and assess whether the constrained projections of future extreme precipitation changes made with the remaining models provide better estimates of pseudo-observations of the future. We assess whether the constrained changes exhibit smaller biases, which are defined as the differences between the best estimates and corresponding pseudo future observations. We consider only grid cells where the adaptive emergent constraint method is applicable to 80% of the considered CMIP6 models. At each such grid cell, we compare the constrained and unconstrained biases using a paired t-test at the 5% significance level.

Similarly, we compare the constrained and unconstrained variances and RMSEs (i.e., the square root of the sum of the square of the projection bias and error variance) to ascertain whether the constrained changes have reduced uncertainty intervals and combinations of bias and uncertainty, respectively.

In addition, to ensure that the narrowed uncertainty intervals are actually not too narrow to include the pseudo future observations, we study the proportion of the constrained 90% uncertainty intervals that cover (include) the pseudo future observations. We expect this coverage rate to be around the nominal value of 90%. A substantially smaller coverage rate would indicate either strongly biased or over constrained projections. It is noted that the cross-validation is implemented on the extreme precipitation changes estimated using spatial and ensemble data aggregation, and thus the evaluation does not count the effects of data aggregation in reducing internal variability uncertainty in externally forced extreme precipitation projections.

Data availability

All data analyzed in this study are publicly available. The HadCRUT5 temperature observations are available at <https://www.metoffice.gov.uk/hadobs/hadcrut5/> and the CMIP6 climate model simulations are available at <https://esgf-node.llnl.gov/search/cmip6/>. The gridded global population data are available at <https://doi.org/10.7927/H4X63JVC>.

Code availability

The code to perform the analysis of this study is available from the corresponding author upon request.

References

- Sun, Q., Zhang, X., Zwiers, F. W., Westra, S. & Alexander, L. V. A global, continental, and regional analysis of changes in extreme precipitation. *J. Clim.* **34**, 243–258 (2021).
- Park, S. et al. Determining the anthropogenic greenhouse gas contribution to the observed intensification of extreme precipitation. *Geophys. Res. Lett.* **47**, e2019GL086875 (2020).
- Dong, S. et al. Attribution of extreme precipitation with updated observations and CMIP6 simulations. *J. Clim.* **34**, 871–881 (2021).
- Li, C. et al. Changes in annual extremes of daily temperature and precipitation in CMIP6 models. *J. Clim.* **34**, 3441–3460 (2021).
- Wehner, M. F. Characterization of long period return values of extreme daily temperature and precipitation in the CMIP6 models: Part 2, projections of future change. *Weather. Clim. Extremes.* **30**, 100284 (2020).
- Chester, M. V., Underwood, B. S. & Samaras, C. Keeping infrastructure reliable under climate uncertainty. *Nat. Clim. Change* **10**, 488–490 (2020).
- Tian, Z. et al. Dynamic adaptive engineering pathways for mitigating floods risks in Shanghai with regret theory. *Nat. Water* **1**, 198–208 (2023).
- Zhang, W., Furtado, K., Zhou, T., Wu, P. & Chen, X. Constraining extreme precipitation projections using past precipitation variability. *Nat. Commun.* **13**, 6319 (2022).
- Paik, S., An, S.-I., Min, S.-K., King, A. & Kim, S.-K. Emergent constraints on future extreme precipitation intensification: from global to continental scales. *Weather Clim. Extrem.* **42**, 100613 (2023).
- Li, C. et al. Constraining projected changes in rare intense precipitation events across global land regions. *Geophys. Res. Lett.* **51**, e2023GL105605 (2024).
- Dai, P., Nie, J., Yu, Y. & Wu, R. Constraints on regional projections of mean and extreme precipitation under warming. *Proc. Natl. Acad. Sci. USA* **121**, e2312400121 (2024).
- Fischer, E. M., Sedláček, J., Hawkins, E. & Knutti, R. Models agree on forced response pattern of precipitation and temperature extremes. *Geophys. Res. Lett.* **41**, 8554–8562 (2014).
- Li, C., Zwiers, F. W., Zhang, X. & Li, G. How much information is required to well constraint local estimates of future precipitation extremes? *Earths Future* **7**, 11–24 (2019).
- Li, C. et al. Larger increases in more extreme local precipitation events as climate warms. *Geophys. Res. Lett.* **46**, 6885–6891 (2019).
- Allen, M. R. & Ingram, W. J. Constraints on future changes in climate and the hydrological cycle. *Nature* **419**, 224–232 (2002).
- Borodina, A., Fischer, E. M. & Knutti, R. Models are likely to underestimate increase in heavy rainfall in the extratropical regions with high rainfall intensity. *Geophys. Res. Lett.* **44**, 7401–7409 (2017).
- Thackeray, C. W., Hall, A., Norris, J. & Chen, D. Constraining the increased frequency of global precipitation extremes under warming. *Nat. Clim. Change* **12**, 441–448 (2022).
- O’Gorman, P. A. Sensitivity of tropical precipitation extremes to climate change. *Nat. Geosci.* **5**, 697–700 (2012).
- Trenberth, K. E. Conceptual framework for changes of extremes of the hydrological cycle with climate change. *Clim. Change* **42**, 327–339 (1999).
- O’Gorman, P. A. & Schneider, T. The physical basis for increases in precipitation extremes in simulations of 21st-century climate change. *Proc. Natl. Acad. Sci. USA* **106**, 14773–14777 (2009).
- Pfahl, S., O’Gorman, P. A. & Fischer, E. M. Understanding the regional pattern of projected future changes in extreme precipitation. *Nat. Clim. Change* **7**, 423–427 (2017).
- Nie, J., Sobel, A. H., Shaevitz, D. A. & Wang, S. Dynamic amplification of extreme precipitation sensitivity. *Proc. Natl. Acad. Sci. USA* **115**, 9467–9472 (2018).
- Nie, J., Dai, P. & Sobel, A. H. Dry and moist dynamics shape regional patterns of extreme precipitation sensitivity. *Proc. Natl. Acad. Sci. USA* **117**, 8757–8763 (2020).
- Huang, Z., Tan, X., Gan, T. Y., Liu, B. & Chen, X. Thermodynamically enhanced precipitation extremes due to counterbalancing influences of anthropogenic greenhouse gases and aerosols. *Nat. Water* **1**, 614–625 (2025).
- Sun, Q., Zwiers, F., Zhang, X. & Tan, Y. The effect of greenhouse gas-induced warming on the impact of El Niño and La Niña events on daily precipitation extremes in the boreal cold season. *J. Clim.* **36**, 6393–6407 (2023).
- Eyring, V. et al. Overview of the Coupled Model Intercomparison Project Phase 6 (CMIP6) experimental design and organization. *Geosci. Model Dev.* **9**, 1937–1958 (2016).
- Zelinka, M. D. et al. Causes of higher climate sensitivity in CMIP6 models. *Geophys. Res. Lett.* **47**, e2019GL085782 (2020).
- Hausfather, Z., Marvel, K., Schmidt, G. A., Nielsen-Gammon, J. & Zelinka, M. Climate simulations: recognize the ‘hot model’ problem. *Nature* **605**, 26–29 (2022).
- Voosen, P. Hot’ climate models exaggerate Earth impacts. *Science* **376**, 685–685 (2022).
- Tokarska, K. B. et al. Past warming trend constrains future warming in CMIP6 models. *Sci. Adv.* **6**, eaaz9549 (2020).
- Ribes, A., Qasmi, S. & Gillett, N. P. Making climate projections conditional on historical observations. *Sci. Adv.* **7**, eabc0671 (2021).
- Liang, Y., Gillett, N. P. & Monahan, A. H. Climate model projections of 21st century global warming constrained using the observed warming trend. *Geophys. Res. Lett.* **47**, e2019GL086757 (2020).
- Liang, Y., Gillett, N. P. & Monahan, A. H. Accounting for Pacific climate variability increases projected global warming. *Nat. Clim. Change* **14**, 608–614 (2024).
- O’Neill, B. C. et al. The Scenario Model Intercomparison Project (ScenarioMIP) for CMIP6. *Geosci. Model Dev.* **9**, 3461–3482 (2016).
- Deser, C., Knutti, R., Solomon, S. & Phillips, A. S. Communication of the role of natural variability in future North America climate. *Nat. Clim. Change* **2**, 775–779 (2012).

36. Hawkins, E. & Sutton, R. The potential to narrow uncertainty in regional climate predictions. *Bull. Am. Meteorol. Soc.* **90**, 1085–1107 (2009).
37. Lehner, F. & Deser, C. Origin, importance, and predictive limits of internal climate variability. *Environ. Res. Climate.* **2**, 023001 (2023).
38. Dai, P. & Nie, J. What controls the interannual variability of extreme precipitation? *Geophys. Res. Lett.* **48**, e2021GL095503 (2021).
39. Holland, M. M. & Bits, C. M. Polar amplification of climate change in coupled models. *Clim. Dynam.* **21**, 221–232 (2003).
40. Zhang, X. et al. Enhanced poleward moisture transport and amplified northern high-latitude wetting trend. *Nat. Clim. Change* **3**, 47–51 (2013).
41. Huang, P. & Xie, S. Mechanisms of changes in ENSO-induced tropical Pacific rainfall variability in a warming climate. *Nat. Geosci.* **8**, 922–926 (2015).
42. Vecchi, G. A. et al. Weakening of tropical Pacific atmospheric circulation due to anthropogenic forcing. *Nature* **441**, 73–76 (2006).
43. Lu, J., Vecchi, G. A. & Reichler, T. Expansion of the Hadley cell under global warming. *Geophys. Res. Lett.* **34**, L06805 (2007).
44. Tamarin-Brodsky, T. & Kaspi, Y. Enhanced poleward propagation of storms under climate change. *Nat. Geosci.* **10**, 908–913 (2017).
45. Bony, S. et al. Robust direct effect of carbon dioxide on tropical circulation and regional precipitation. *Nat. Geosci.* **6**, 447–451 (2013).
46. Sillmann, J., Stjern, C. W., Myhre, G. & Forster, P. M. Slow and fast responses of mean and extreme precipitation to different forcing in CMIP5 simulations. *Geophys. Res. Lett.* **44**, 6383–6390 (2017).
47. Xue, D. et al. Robust projection of East Asian summer monsoon rainfall based on dynamical models of variability. *Nat. Commun.* **14**, 3856 (2023).
48. Moon, S. et al. Anthropogenic warming induced intensification of summer monsoon frontal precipitation over East Asia. *Sci. Adv.* **9**, eadh4195 (2023).
49. Hegerl, G. C. et al. Challenges in quantifying changes in the global water cycle. *Bull. Am. Meteorol. Soc.* **96**, 1097–1115 (2015).
50. Mitchell, D. et al. Realizing the impacts of 1.5 °C warmer world. *Nat. Clim. Change* **6**, 735–737 (2016).
51. Lee, D., Sparrow, S. N., Min, S.-K., Yeh, S.-W. & Allen, M. R. Physically based equation representing the forcing-driven precipitation in climate models. *Environ. Res. Lett.* **18**, 094063 (2023).
52. Lin, L., Wang, Z., Xu, Y. & Fu, Q. Sensitivity of precipitation extremes to radiative forcing of greenhouse gases and aerosols. *Geophys. Res. Lett.* **43**, 9860–9868 (2016).
53. Wang, Z. et al. Scenario dependence of future changes in climate extremes under 1.5 °C and 2 °C global warming. *Sci. Rep.* **7**, 46432 (2017).
54. Sillmann, J. et al. Extreme wet and dry conditions affected differently by greenhouse gases and aerosols. *NPJ Clim.* **2**, 24 (2019).
55. Pendergrass, A. G., Lehner, F., Sanderson, B. M. & Xu, Y. Does extreme precipitation intensity depend on the emissions scenario? *Geophys. Res. Lett.* **42**, 8767–8774 (2015).
56. Hall, A., Cox, P., Huntingford, C. & Klein, S. Progressing emergent constraints on future climate change. *Nat. Clim. Change* **9**, 269–278 (2019).
57. Tebaldi, C., Arblaster, J. M. & Knutti, R. Mapping model agreement on future climate projections. *Geophys. Res. Lett.* **38**, L23701 (2011).
58. Sanderson, B. M., Knutti, R. & Caldwell, P. Addressing interdependency in a multimodel ensemble by interpolation of model properties. *J. Clim.* **28**, 5150–5170 (2015).
59. Annan, J. D. & Hargreaves, J. C. Reliability of the CMIP3 ensemble. *Geophys. Res. Lett.* **37**, L02703 (2010).
60. Morice, C. P. et al. An updated assessment of near-surface temperature change from 1850: the HadCRUT5 data set. *J. Geophys. Res. Atmos.* **126**, e2019JD032361 (2021).
61. Jiménez-de-la-Cuesta, D. & Mauritsen, T. Emergent constraints on Earth's transient and equilibrium response to doubled CO₂ from post-1970s global warming. *Nat. Geosci.* **12**, 902–905 (2019).
62. Watanabe, M. et al. Possible shift in controls of the tropical Pacific surface warming pattern. *Nature* **630**, 315–324 (2024).
63. Gulev, S. K., et al. Changing State of the Climate System. in *Climate Change 2021: The Physical Science Basis* (eds Masson-Delmotte, V., et al.) Ch. 2 (Cambridge Univ. Press, 2021).
64. Lee, J.-Y. et al., Future Global Climate: Scenario-Based Projections and Near-Term Information. in *Climate Change 2021: The Physical Science Basis*, (eds Masson-Delmotte, V., et al.) Ch. 4 (Cambridge Univ. Press, 2021).
65. Zhou, T., Lu, J., Zhang, W. & Chen, Z. The sources of uncertainty in the projection of global land monsoon precipitation. *Geophys. Res. Lett.* **47**, e2020GL088415 (2020).
66. Juzbašić, A. et al. The difference in the uncertainty sources between future projections of mean and extreme precipitation over East Asia. *Environ. Res. Lett.* **19**, 074015 (2024).
67. Center for International Earth Science Information Network - CIESIN - Columbia University. Gridded population of the world, Version 4 (GPWv4): population count. NASA Socioeconomic Data and Applications Center (SEDAC). <https://doi.org/10.7927/H4X63JVC> (2016). Accessed 23 September 2024.
68. Risser, M. D. et al. Anthropogenic aerosols mask increases in US rainfall by greenhouse gases. *Nat. Commun.* **15**, 1318 (2024).
69. Deser, C. et al. Insights from Earth system model initial-condition large ensembles and future prospects. *Nat. Clim. Change* **10**, 277–286 (2020).
70. Bowman, K. W., Cressie, N., Qu, X. & Hall, A. A hierarchical statistical framework for emergent constraints: application to snow-albedo feedback. *Geophys. Res. Lett.* **45**, 13050–13059 (2018).
71. von Storch, H. & Zwiers, F. W. *Statistical Analysis in Climate Research* (Cambridge University Press, 1999).

Acknowledgements

We thank the World Climate Research Programme's Working Group on Coupled Modeling and the individual modeling groups for their roles in making CMIP data available. C.L. and F.D. are supported by National Key R&D Program of China (2020YFA0608901) and National Natural Science Foundation of China (42075026).

Author contributions

C.L. and F.Z. designed the study with input from G.F. J.L. led the computation with assistance from C.L. and F.D. C.L. and F.Z. wrote the initial draft. C.L., J.L., F.D., F.Z., and G.F. interpreted the results and edited the manuscript.

Competing interests

The authors declare no competing interests.

Additional information

Supplementary information The online version contains supplementary material available at <https://doi.org/10.1038/s41467-025-56235-9>.

Correspondence and requests for materials should be addressed to Chao Li.

Peer review information *Nature Communications* thanks the anonymous reviewers for their contribution to the peer review of this work. A peer review file is available.

Reprints and permissions information is available at <http://www.nature.com/reprints>

Publisher's note Springer Nature remains neutral with regard to jurisdictional claims in published maps and institutional affiliations.

Open Access This article is licensed under a Creative Commons Attribution-NonCommercial-NoDerivatives 4.0 International License, which permits any non-commercial use, sharing, distribution and reproduction in any medium or format, as long as you give appropriate credit to the original author(s) and the source, provide a link to the Creative Commons licence, and indicate if you modified the licensed material. You do not have permission under this licence to share adapted material derived from this article or parts of it. The images or other third party material in this article are included in the article's Creative Commons licence, unless indicated otherwise in a credit line to the material. If material is not included in the article's Creative Commons licence and your intended use is not permitted by statutory regulation or exceeds the permitted use, you will need to obtain permission directly from the copyright holder. To view a copy of this licence, visit <http://creativecommons.org/licenses/by-nc-nd/4.0/>.

© The Author(s) 2025